Probing the Optical Properties and Strain-Tuning of Ultrathin Mo$_{1-x}$W$_x$Te$_2$

Ozgur Burak Aslan,[*,†,⊥] Isha M. Datye,[‡] Michal J. Mleczko,[‡] Karen Sze Cheung,[†] Sergiy Krylyuk,[#,∇] Alina Bruma,[#] Irina Kalish,[#] Albert V. Davydov,[#] Eric Pop,[*,‡,§,∥] and Tony F. Heinz[*,†,⊥]

[†]Department of Applied Physics, [‡]Department of Electrical Engineering, [§]Department of Materials Science and Engineering, and [∥]Precourt Institute for Energy, Stanford University, Stanford, California 94305, United States

[⊥]SLAC National Accelerator Laboratory, Menlo Park, California 94025, United States
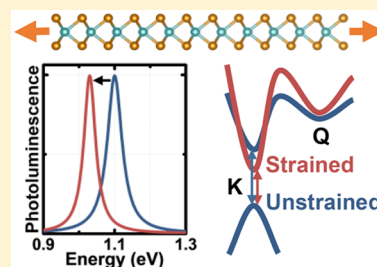
[#]Material Measurement Laboratory, National Institute of Standards and Technology, Gaithersburg, Maryland 20899, United States

[∇]Theiss Research, La Jolla, California 92037, United States

Ⓢ *Supporting Information*

ABSTRACT: Ultrathin transition metal dichalcogenides (TMDCs) have recently been extensively investigated to understand their electronic and optical properties. Here we study ultrathin Mo$_{0.91}$W$_{0.09}$Te$_2$, a semiconducting alloy of MoTe$_2$, using Raman, photoluminescence (PL), and optical absorption spectroscopy. Mo$_{0.91}$W$_{0.09}$Te$_2$ transitions from an indirect to a direct optical band gap in the limit of monolayer thickness, exhibiting an optical gap of 1.10 eV, very close to its MoTe$_2$ counterpart. We apply tensile strain, for the first time, to monolayer MoTe$_2$ and Mo$_{0.91}$W$_{0.09}$Te$_2$ to tune the band structure of these materials; we observe that their optical band gaps decrease by 70 meV at 2.3% uniaxial strain. The spectral widths of the PL peaks decrease with increasing strain, which we attribute to weaker exciton−phonon intervalley scattering. Strained MoTe$_2$ and Mo$_{0.91}$W$_{0.09}$Te$_2$ extend the range of band gaps of TMDC monolayers further into the near-infrared, an important attribute for potential applications in optoelectronics.

KEYWORDS: *MoTe$_2$, MoWTe$_2$, band gap, strain engineering, alloyed 2D materials, photoluminescence*

Atomically thin layers of transition metal dichalcogenides (TMDCs), such as MoTe$_2$, have been extensively studied for fundamental physics and applications.[1,2] Tuning their optical properties, which can be achieved through doping, alloying, strain, or heating, is crucial for understanding their light−matter interactions and for various applications in electronics and optoelectronics. The optical properties of atomically thin MoTe$_2$ have recently been characterized experimentally,[3−7] and theoretical investigations have indicated that the aforementioned factors can significantly alter the material's band structure.[8−12] In particular, theory has predicted and measurements have demonstrated that alloying with tungsten or electrical gating of MoTe$_2$ can induce a phase change from a semiconducting to metallic state.[8,9,13−16] To date, however, few studies have experimentally examined the effects of strain on MoTe$_2$ or on MoWTe$_2$ alloys.[17]

Here we investigate Mo$_{1-x}$W$_x$Te$_2$ with x = 0.09 since for alloys with higher W content, *i.e.*, x > 0.09, all reported growth processes have produced crystals in the 1T′ phase. Therefore, this composition is close to the 2H phase boundary and should exhibit the lowest threshold for inducing a 2H to 1T′ phase change by an external perturbation.[15,18,19] We study atomically thin crystals of the Mo$_{0.91}$W$_{0.09}$Te$_2$ alloy by Raman scattering, photoluminescence (PL), and absorption measurements, and compare the results with those for MoTe$_2$. We also measure PL while applying in-plane uniaxial tensile strain to the monolayer

(1L) crystals of both compounds to alter their band structure, which has not been previously examined.

We have grown bulk MoTe$_2$ and Mo$_{1-x}$W$_x$Te$_2$ crystals using the chemical vapor transport (CVT) method, as detailed in the Supporting Information (SI) sections 1.1 and 1.2. The 2H crystal structure of Mo$_{0.91}$W$_{0.09}$Te$_2$ has been confirmed by powder X-ray diffraction (XRD), as shown in Figure 1a (see Figure S1 in the SI section 1.3 for an extended version of the XRD data), and by scanning transmission electron microscopy (STEM) (Figure 1b). The W mole fraction in the Mo$_{1-x}$W$_x$Te$_2$ alloy, as determined from X-ray energy dispersive spectroscopy (EDS), is x = 0.09 ± 0.01 (see Figure S2). For optical measurements, we have exfoliated atomically thin layers from the grown bulk MoTe$_2$ and Mo$_{0.91}$W$_{0.09}$Te$_2$ crystals (see the SI section 1.4, Figure S3, and the SI section 2 for details on the sample preparation and optical measurement setup).

We first perform Raman spectroscopy on Mo$_{0.91}$W$_{0.09}$Te$_2$ and MoTe$_2$ crystals exfoliated on polydimethylsiloxane (PDMS) substrates. Here and below all characterization measurements have been performed at room temperature and under ambient conditions. Figure 2 shows the Raman spectra of 1L, bilayer (2L), trilayer (3L), four-layer (4L), and bulk Mo$_{0.91}$W$_{0.09}$Te$_2$
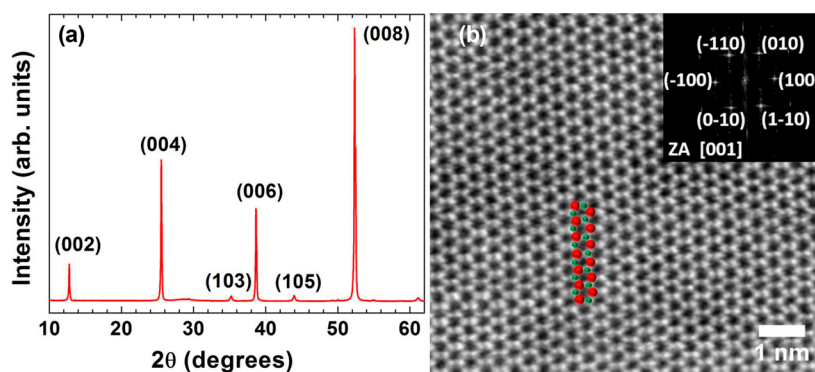
Figure 1. (a) Powder XRD pattern of 2H−Mo$_{0.91}$W$_{0.09}$Te$_2$. (b) High angle annular dark field scanning electron microscopy (HAADF-STEM) image of a 2H−Mo$_{0.91}$W$_{0.09}$Te$_2$ sample together with an overlapped structural model: red (large) spheres, Mo/W atoms; green (small) spheres, Te atoms. Inset: fast Fourier transform (FFT) emphasizing the [001] zone axis.
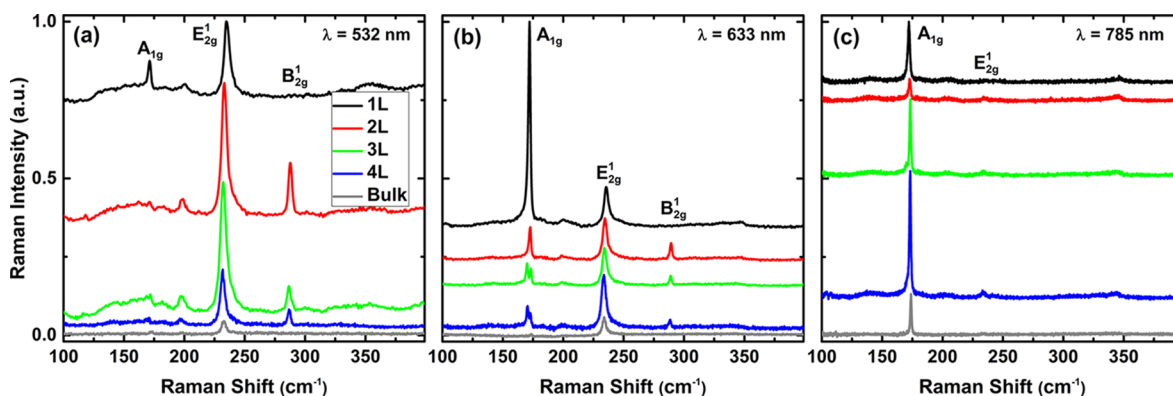

Figure 2. Raman spectra of 1L to 4L and bulk Mo$_{0.91}$W$_{0.09}$Te$_2$ (modes labeled according to bulk notation) for excitation wavelengths of (a) 532, (b) 633, and (c) 785 nm. The spectra are vertically offset for clarity.
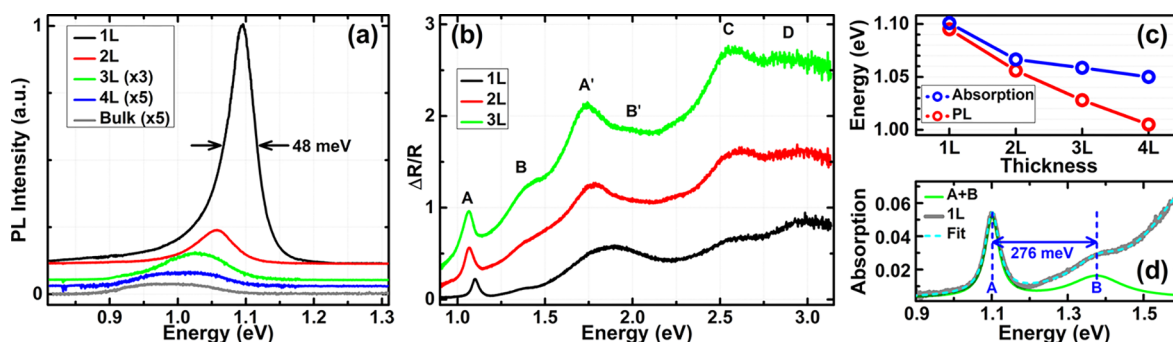

Figure 3. (a) PL spectra of 1L to 4L and bulk Mo$_{0.91}$W$_{0.09}$Te$_2$. The 1L to 4L spectra are vertically offset for clarity. Black arrows indicate the width of 48 meV of the 1L spectrum. (b) Reflection contrast ($\Delta R/R$) spectra for 1L to 3L Mo$_{0.91}$W$_{0.09}$Te$_2$. (c) Comparison of the A exciton and PL peak positions as a function of crystal thickness. (d) Absorption spectrum for the 1L in the near-IR, shown in terms of absorption for a free-standing layer. The green curve shows the contributions of the A and B excitons to the spectrum based on a fit (dotted line) to the experimental data.

crystals for excitation wavelengths of 532, 633, and 785 nm (see Figure S4 for the MoTe$_2$ spectra). We note that the relatively small band gaps of ultrathin MoTe$_2$ and Mo$_{0.91}$W$_{0.09}$Te$_2$ (see the section on PL) compared to other TMDCs enable the use of longer excitation wavelengths for resonant Raman spectroscopy.[3,20,21] We identify the following first-order Raman modes (zone-center phonons) in both materials: the out-of-plane A$_{1g}$ (A$_1'$ for odd, A$_{1g}$ for even layers), in-plane E$_{2g}^1$ (E′ for odd, E$_g$ for even layers), and out-of-plane B$_{2g}^1$ (A$_2''$ for 1L, A$_1'$ for odd, A$_{1g}$ for even layers), which is Raman inactive in 1L and bulk crystals.[3,19,21−27] For 1L Mo$_{0.91}$W$_{0.09}$Te$_2$, the A$_{1g}$ mode is at 172 cm^{-1}, and the E$_{2g}^1$ mode appears at 236 cm^{-1}. The weaker

features at 200 and 345 cm^{-1} have recently been attributed to second-order Raman processes[21] and appear to be stronger in Mo$_{0.91}$W$_{0.09}$Te$_2$ than in MoTe$_2$, possibly due to changes in the electronic structure with the addition of W.

After comparing the Raman spectra of the two materials, we observe that the A$_{1g}$ and E$_{2g}^1$ modes of Mo$_{0.91}$W$_{0.09}$Te$_2$ are slightly blueshifted, and the B$_{2g}^1$ mode is slightly redshifted from those of MoTe$_2$ for 1L and 2L (see Table S1 for the Raman peak positions of both materials). We explain these observations as follows. Consider a simplified linear triatomic molecule model for which interlayer interactions in the 1L and 2L have little effect (e.g., no splitting of the E$_{2g}^1$ mode). We then

expect the increased W content in $Mo_{0.91}W_{0.09}Te_2$ to increase the effective mass of the transition metal atoms and to result accordingly in a redshift of modes compared to $MoTe_2$.[28] This was reported for the E_{2g}^1 and B_{2g}^1 modes in alloys of Mo and W dichalcogenides (e.g., $Mo_{1-x}W_xS_2$ and $Mo_{1-x}W_xSe_2$).[29−33] We observe this redshift in the B_{2g}^1 mode and the second-order Raman mode at 200 cm^{-1}. However, the frequency of the A_{1g} mode depends more on bond strength than on mass of the transition metal, since this atom remains stationary in this vibrational mode.[22] Since W−Te bonds are stronger than Mo−Te bonds,[34] adding W to $MoTe_2$ stiffens the bonds, leading, as in other TMDC alloys,[31−33] to a blueshift of the A_{1g} mode. Interestingly, in contrast to other TMDC alloys,[30−33] we observe a blueshift of the E_{2g}^1 mode for 1L and 2L of the alloy compared to the $MoTe_2$ crystal. This blueshift also results from the increased bond strength, which apparently outweighs the influence of the increase in mass.

Next, we examine the relative intensities of the Raman modes for different layer thicknesses in both materials. For 532 nm excitation, for both $MoTe_2$ and $Mo_{0.91}W_{0.09}Te_2$ crystals of all thicknesses, the E_{2g}^1 mode is stronger than all other modes. The A_{1g} mode is strongest for 1L and becomes much weaker with increasing thickness (Figure 2a, Figure S4a). For 633 nm excitation, the A_{1g} mode is enhanced compared to the E_{2g}^1 mode for 1L samples of both materials. We attribute the strength of this mode to a resonance effect associated with the excitation photon energy being close to that of the A′ or B′ excitons in the material (see Figure 3 for the A′ and B′ peak positions).[25,26] For 2L crystals, the A_{1g} and B_{2g}^1 modes are comparable in intensity, but weaker than the E_{2g}^1 mode. For 3L and 4L crystals, the A_{1g} mode splits into 2 peaks [$A_{1g}(R1)$ and $A_{1g}(R2)$], known as Davydov splitting,[25,35] which are stronger than the B_{2g}^1 mode (see Figure 2b). The ratio of the B_{2g}^1 to E_{2g}^1 mode can also be used to identify thickness in few-layer crystals using both 532 and 633 nm excitation.[4,23]

Using 785 nm excitation, we observe that the E_{2g}^1 mode is much weaker than the A_{1g} mode for all layer thicknesses. For the thicknesses we have measured, the A_{1g} mode is weakest for 2L and strongest for 4L crystals in both $Mo_{0.91}W_{0.09}Te_2$ and $MoTe_2$ (see Figure 2c and Figure S4c). The reason for this nonmonotonic change of the intensity of the A_{1g} mode with increasing thickness is unclear. The B_{2g}^1 mode does not appear in the 785 nm Raman spectra for any crystal thickness, as in the case of MoS_2 and $MoSe_2$ for excitation energies far from the C electronic resonance (see Figure 3 for the C peak position).[24,36] Calculations have shown that the A and B excitons have wave functions that are mainly confined to the individual layers,[24,36] and it has been predicted that for excitation energies near the A and B excitons, the active B_{2g}^1 mode of the few-layer crystals is inactive, as it is for 1L crystals. However, the wave function associated with the C transition is calculated to be not confined to individual layers.[37,38] Hence, excitation nearer to the C feature, in this case 532 and 633 nm, yields Raman spectra with stronger B_{2g}^1 modes. The comparisons of the Raman spectra with three different excitation wavelengths presented here provide a rapid means of determining the thickness of ultrathin layers of $Mo_{0.91}W_{0.09}Te_2$ and $MoTe_2$.

We perform PL measurements in order to study the band structure of $Mo_{0.91}W_{0.09}Te_2$. Figure 3a displays the PL spectra of 1L to 4L and bulk $Mo_{0.91}W_{0.09}Te_2$ supported on PDMS substrates. We see that the PL intensity decreases, that the peak position redshifts, and that the spectral width (full width at half-maximum) increases with increasing layer thickness. The 1L

spectrum exhibits a single emission peak, with the maximum located at 1.10 eV and a width of 48 meV. The width of the 2L is 20 meV greater than that of the 1L. For the bulk, we find a much broader and weaker PL feature peaked at 0.98 eV.

In order to comment on the nature of the peaks observed in the PL spectra and understand the changes with increasing material thickness, we also measure the reflection contrast ($\Delta R/R$) spectra of 1L to 3L $Mo_{0.91}W_{0.09}Te_2$ on PDMS substrates, as displayed in Figure 3b, to probe their absorption spectra (see the SI section 2 for details on the reflection contrast measurements). We expect to observe only direct optical transitions in the reflection contrast spectrum since the indirect transitions produce only weak contributions to the absorption spectrum. Several features are observed in the spectra of Figure 3b, and we expect them to arise from mechanisms similar to those in $MoTe_2$. Thus, we have labeled them according to the bulk assignments of Wilson and Yoffe[39] as was previously done for the case of $MoTe_2$.[3] These spectroscopic features are associated with transitions in different parts of the Brillouin zone of $Mo_{0.91}W_{0.09}Te_2$. The A, B and A′, B′ pairs have been identified as excitonic transitions with the A−B splitting arising from spin−orbit interactions.[39,40] As for other TMDC monolayers, the A and B peaks are assigned to excitonic peaks associated with the lowest direct optical transition at the K-point.[41−43] The C and D features have been attributed to regions of parallel bands near the Γ point of the Brillouin zone of bulk $MoTe_2$[44] and to similar parallel bands in monolayers of other TMDCs.[37,45]

We now compare the PL and reflection contrast response of $Mo_{0.91}W_{0.09}Te_2$ for different thicknesses. Figure 3b shows that the reflection contrast increases, and the A exciton redshifts with increasing thickness. The PL spectra in Figure 3a show that the peak position also redshifts; however, the rate of the redshift of the PL peak is faster than that of the A exciton, and the intensity of the PL peak decreases as opposed to that of the A exciton. We report the position of the A exciton and the PL peak position as a function of thickness in Figure 3c. The A exciton redshifts by 33 meV to 1.067 eV from 1L to 2L and continues shifting gradually with increasing thickness. However, the PL peaks redshift more than the A exciton peaks; the two peaks are separated by 5 meV for 1L, but by 45 meV for 4L.

We attribute this large difference in the shift between the absorption and emission features to the emergence of an indirect transition at lower energies than the A exciton with increasing thickness, as observed in other semiconducting TMDCs.[46,47] We expect the indirect band gap to contribute to PL, but not significantly to the absorption spectrum. We thus conclude that 1L $Mo_{0.91}W_{0.09}Te_2$ exhibits a direct band gap, unlike the crystals thicker than 2L, in accordance with the behavior of its $MoTe_2$ counterpart. The PL intensity of the 1L crystal is about 3 orders of magnitude greater than that of the bulk, due to the direct optical gap transition of the former. Even though the PL intensity is significantly weaker for 2L than it is for 1L, since the PL peak and the A exciton are separated by only 10 meV, the assignment of the 2L material as indirect gap is unclear. However, the 20 meV increase in the width of the PL and A exciton peaks of 2L as compared to 1L strongly indicates the presence of a scattering channel for the A exciton in the 2L. We also note that there have been different opinions on the nature of the 2L $MoTe_2$ band gap, at both room[3,5] and low temperatures.[4]

The near-IR part of the 1L absorption spectrum is shown in greater detail in Figure 3d. We find that the A and B features
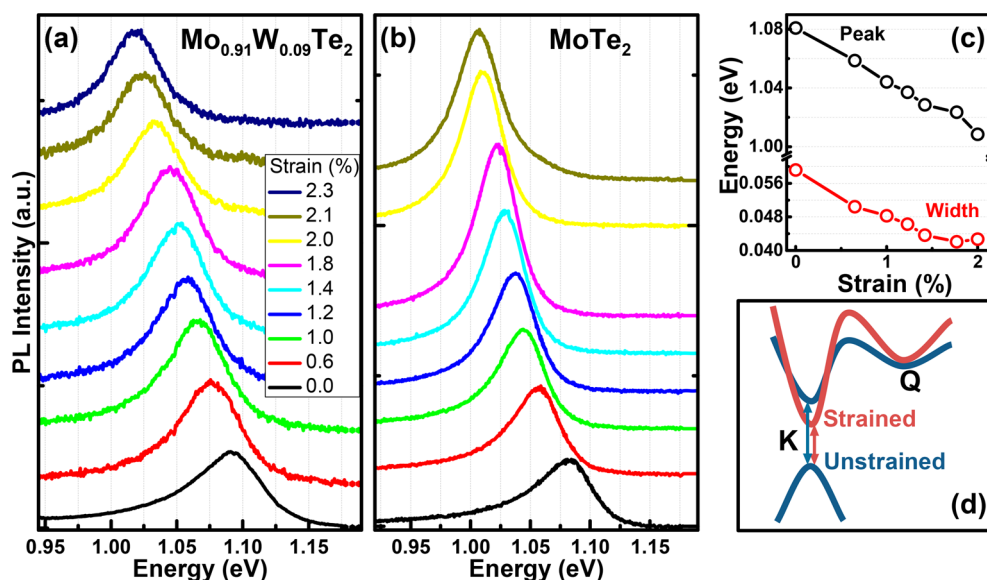
Figure 4. PL spectra of 1L (a) $Mo_{0.91}W_{0.09}Te_2$ and (b) $MoTe_2$ under different amounts of uniaxial tensile strain. All spectra are vertically offset for clarity. (c) Dependence of the peak energy and spectral width of 1L $MoTe_2$ on strain. (d) Schematic band structure of strained and unstrained 1L $MoTe_2$, showing changes in the energy separation between the minima of the K and Q valleys in the conduction band.

are located at 1.10 and 1.38 eV, respectively. The corresponding features appear at similar energies of 1.10 and 1.35 eV, respectively, for 1L $MoTe_2$.[3] We note that the direct gap, or A exciton, position in $Mo_{0.91}W_{0.09}Te_2$ is not very different from that of $MoTe_2$, which is consistent with the observation that, for a given chalcogen (S, Se), the band gaps of Mo and W dichalcogenides are quite similar.[20] The A−B splitting for 1L is found to be 276 meV, which is slightly greater than the $MoTe_2$ value of 250 meV.[3] We attribute this increase to the presence of W, since dichalcogenides of W have significantly higher A−B splitting than those of Mo.[20,48,49]

To gain further insight into the band structure of 1L $MoTe_2$ and $Mo_{0.91}W_{0.09}Te_2$, we perform strain-dependent PL measurements on these materials. We apply uniaxial in-plane tensile strain to a flexible substrate using a two-point bending apparatus (see the SI section 1.4 and Figure S3 for more details). We used PEN (polyethylene naphthalate) or PETG (polyethylene terephthalate glycol-modified) instead of PDMS for the bending platform (Figure S3), due to their higher Young's moduli. Figures 4a,b show the PL measurements of 1L $Mo_{0.91}W_{0.09}Te_2$ and $MoTe_2$ as a function of strain. As the strain increases, the PL peak redshifts, corresponding to a decrease in the band gap. For $Mo_{0.91}W_{0.09}Te_2$, the PL peak shifts from 1.09 eV at 0% strain to 1.02 eV at 2.3% strain or −30 meV/% strain. For $MoTe_2$, the PL peak shifts from 1.08 eV at 0% strain to 1.01 eV at 2.1% strain or −33 meV/% strain. We note that these values of strain and the rates of peak shift with strain are reasonable, as discussed in the SI section 4 and shown in Figure S5. The widths of the $Mo_{0.91}W_{0.09}Te_2$ and $MoTe_2$ PL peaks decrease from 63 and 59 meV, respectively, at 0% strain to minimum values of 49 and 42 meV, respectively, with strain. Figure 4c shows how the 1L $MoTe_2$ PL peak energy and spectral widths vary with strain (see the SI Figure S6a for the $Mo_{0.91}W_{0.09}Te_2$ results).

To account for the unexpected decrease of the width of the emission peak in the PL spectra with increasing strain for both materials, we can identify three possible factors: (1) The contribution to PL from trions is suppressed. (2) The material conforms better to the flexible substrate (after being trans-

ferred), reducing inhomogeneous broadening. (3) Exciton−phonon scattering is partially suppressed.

We first consider the suppression of trion emission due to strain. Trions are not expected to contribute much to absorption unless the sample is heavily doped.[50,51] However, trions can still contribute appreciably to PL since they are more stable even at room temperature due to their high binding energy of about 25 meV.[6,7] Therefore, if suppression of trion PL caused the reduction in the line width, we would not expect to see a parallel narrowing in the absorption feature with strain. However, our measurements show a similar decrease in the width of the absorption and PL features, thus ruling out this mechanism (see the SI section 6 and Figures S7 and S8).

Second, we consider the possibility that the material conforms better to the substrate under strain, leading to a reduction of inhomogeneous broadening. We first observe that the width of the emission feature of strained 1Ls drops to a value as low as 42 meV (Figure 4c), which is less than that of any as-exfoliated samples (for which the width is around 47−50 meV).[3,5] Further, similar measurements on 1L WSe_2 by Schmidt et al. have demonstrated that the strain-induced narrowing of the spectral widths is reversible upon the release of strain.[52] This observation suggests that the elimination of inhomogeneities alone cannot account for line narrowing in their case, as the inhomogeneities are not expected to recover fully when the strain is released. Hence, we do not expect this mechanism to explain our observations.

Third, we consider the effect of strain on the exciton−phonon coupling. As we know from the current and earlier studies, 1Ls of both materials have direct optical gaps.[3−5,53] However, the 1L has an indirect transition at a slightly higher energy than that of the A exciton, which is known from band structure calculations and from extrapolating the energy of the indirect gap as compared to that of 2L and thicker crystals.[3−5,53] Moreover, the energy separation between the minima of indirect Q (also known as T)[54,55] and direct K valleys, ΔE_{QK}, in the conduction band will increase with uniaxial (as well as biaxial) strain in similar material systems.[11,12,56−58] This is illustrated in Figure 4d, which

shows a schematic band structure of strained and unstrained 1L MoTe$_2$. However, scattering of an electron from the K to Q valley requires the absorption of a phonon. This becomes less likely with increasing ΔE_{QK}. Therefore, we infer from our results that a weakening in the exciton−phonon intervalley scattering is mainly responsible for the decrease in the spectral line widths. We attribute at least 6 meV of the width of the emission feature in the unstrained material to the exciton−phonon scattering from K to Q (Γ_{QK}). We also estimate an upper limit of 110 fs for the lifetime of the exciton−phonon scattering from K to Q in 1L MoTe$_2$ and Mo$_{0.91}$W$_{0.09}$Te$_2$ (see the SI section 6). The ability to suppress phonon absorption indicates that Q and K states are within a few times the phonon energy, and the highest energy phonon to mediate such scattering [the LO(E′) mode] is about 30 meV.[21,54,59] Thus, we predict that ΔE_{QK} of the unstrained 1Ls is not much larger than 30 meV. We expect the line width narrowing effect via tensile strain to be smaller (larger) for MoS$_2$ (WSe$_2$ and WS$_2$), for which ΔE_{QK} is predicted to be larger (smaller) than that in MoTe$_2$.[54,59]

Here we note an advantage of a strain-dependent study over a temperature-dependent one. Strain, like temperature, can modify the band structure, but in the former case without significantly affecting the population of phonons. We also note that it is typically assumed that the relative energy of different valleys is not affected by temperature. This is not always correct as lowering the temperature has a similar effect to biaxial compressive strain.[60] Therefore, tuning the bands of nearly direct or indirect gap semiconductors via strain will provide more insight about the band structure and can help interpret the temperature-dependent studies on the spectral line widths of TMDCs.[6,52,61,62]

Finally, we would like to consider the implications of weaker exciton−phonon scattering for electron transport. There have been calculations of the enhancement of transport properties in group VI TMDCs due to the change in the relative energies of K and Q valleys in the conduction band under tensile strain, leading to a reduction in electron−phonon scattering.[11,63] We propose that this effect should be larger for MoTe$_2$ than MoS$_2$, as the former has a smaller value for ΔE_{QK}. A similar phenomenon has been exploited to enhance the electron mobility of silicon transistors, where the intervalley energy separation increases with tensile strain, leading to reduced intervalley electron−phonon scattering.[64,65] (SI section 7 shows preliminary electrical transport measurements in MoTe$_2$ and MoWTe$_2$, but strain-dependent electrical measurements are beyond the scope of this study.)

In summary, we have characterized single-crystal 2H−Mo$_{0.91}$W$_{0.09}$Te$_2$ down to monolayer thickness with photoluminescence, absorption, and Raman spectroscopy. We have determined that atomically thin 2H−Mo$_{0.91}$W$_{0.09}$Te$_2$ is a semiconductor with similar optical properties to MoTe$_2$; the monolayer possesses a direct optical band gap at 1.10 eV, and the thicker layers become indirect. The presence of W in the alloy alters the band structure, as observed by absorption measurements, and can be studied further by Raman spectroscopy, particularly using resonant excitation.[66] Given that this alloy is closest in W content to the 2H to 1T′ phase transition,[19] it may be a promising material for phase-change memory applications. We have manipulated the band structure of monolayer MoTe$_2$ and Mo$_{0.91}$W$_{0.09}$Te$_2$ via tensile strain up to 2.3% and have thereby lowered the optical band gap of these materials to near 1 eV. We have thus extended the optical range

of group VI TMDC monolayers further into the near-infrared (NIR) region. We have also observed that the relative energy separation between valleys changes with strain, and that exciton−phonon intervalley scattering can also be manipulated in this fashion. We attribute the reduced spectral line width of the A exciton under tensile strain to a decrease in the rate of exciton−phonon scattering. This suggests a corresponding decrease in the electron−phonon scattering rate and a potential improvement in the electrical transport properties in these materials with tensile strain.

■ ASSOCIATED CONTENT

ⓢ Supporting Information

The Supporting Information is available free of charge on the ACS Publications website at DOI: 10.1021/acs.nanolett.8b00049.

Growth, characterization, and preparation of samples; details on the optical measurements; Raman spectroscopy of MoTe$_2$; rate of band gap shift with strain; peak positions and widths of strain-dependent PL measurements on 1L MoTe$_2$ and Mo$_{0.91}$W$_{0.09}$Te$_2$; strain-dependent absorption and PL measurements on 1L Mo$_{0.91}$W$_{0.09}$Te$_2$; and comparison of electrical transport properties of few-layer Mo$_{0.91}$W$_{0.09}$Te$_2$ and MoTe$_2$ (PDF)

■ AUTHOR INFORMATION

Corresponding Authors
*E-mail: oba2002@stanford.edu.
*E-mail: epop@stanford.edu.
*E-mail: tony.heinz@stanford.edu.

ORCID ⓘ
Ozgur Burak Aslan: 0000-0002-0925-3026
Irina Kalish: 0000-0003-0285-9823
Eric Pop: 0000-0003-0436-8534
Tony F. Heinz: 0000-0003-1365-9464

Author Contributions
O.B.A. and I.M.D. contributed equally. The manuscript was written through contributions of all authors. All authors have given approval to the final version of the manuscript.

Notes
Certain commercial equipment, instruments, or materials are identified in this paper in order to specify the experimental procedure adequately. Such identification is not intended to imply recommendation or endorsement by the National Institute of Standards and Technology, nor is it intended to imply that the materials or equipment identified are necessarily the best available for the purpose.
The authors declare no competing financial interest.

■ REFERENCES

(1) Novoselov, K. S.; Jiang, D.; Schedin, F.; Booth, T. J.; Khotkevich, V. V.; Morozov, S. V.; Geim, A. K. Two-Dimensional Atomic Crystals. *Proc. Natl. Acad. Sci. U. S. A.* **2005**, *102*, 10451−3.

(2) Chhowalla, M.; Shin, H. S.; Eda, G.; Li, L. J.; Loh, K. P.; Zhang, H. The chemistry of two-dimensional layered transition metal dichalcogenide nanosheets. *Nat. Chem.* **2013**, *5*, 263−75.

(3) Ruppert, C.; Aslan, O. B.; Heinz, T. F. Optical Properties and Band Gap of Single- and Few-layer $MoTe_2$ Crystals. *Nano Lett.* **2014**, *14*, 6231−6.

(4) Lezama, I. G.; Arora, A.; Ubaldini, A.; Barreteau, C.; Giannini, E.; Potemski, M.; Morpurgo, A. F. Indirect-to-Direct Band Gap Crossover in Few-Layer $MoTe_2$. *Nano Lett.* **2015**, *15*, 2336−42.

(5) Froehlicher, G.; Lorchat, E.; Berciaud, S. Direct versus indirect band gap emission and exciton-exciton annihilation in atomically thin molybdenum ditelluride ($MoTe_2$). *Phys. Rev. B: Condens. Matter Mater. Phys.* **2016**, *94*, 085429.

(6) Koirala, S.; Mouri, S.; Miyauchi, Y.; Matsuda, K. Homogeneous linewidth broadening and exciton dephasing mechanism in $MoTe_2$. *Phys. Rev. B: Condens. Matter Mater. Phys.* **2016**, *93*, 075411.

(7) Yang, J.; Lu, T. Y.; Myint, Y. W.; Pei, J. J.; Macdonald, D.; Zheng, J. C.; Lu, Y. R. Robust Excitons and Trions in Monolayer $MoTe_2$. *ACS Nano* **2015**, *9*, 6603−9.

(8) Li, Y.; Duerloo, K. A. N.; Wauson, K.; Reed, E. J. Structural semiconductor-to-semimetal phase transition in two-dimensional materials induced by electrostatic gating. *Nat. Commun.* **2016**, *7*, 10671.

(9) Duerloo, K. A. N.; Reed, E. J. Structural Phase Transitions by Design in Monolayer Alloys. *ACS Nano* **2016**, *10*, 289−97.

(10) Duerloo, K. A. N.; Li, Y.; Reed, E. J. Structural phase transitions in two-dimensional Mo- and W-dichalcogenide monolayers. *Nat. Commun.* **2014**, *5*, 4214.

(11) Hosseini, M.; Elahi, M.; Pourfath, M.; Esseni, D. Very large strain gauges based on single layer $MoSe_2$ and WSe_2 for sensing applications. *Appl. Phys. Lett.* **2015**, *107*, 253503.

(12) Villegas, C. E. P.; Rocha, A. R. Elucidating the Optical Properties of Novel Heterolayered Materials Based on $MoTe_2$-InN for Photovoltaic Applications. *J. Phys. Chem. C* **2015**, *119*, 11886−95.

(13) Berry, J.; Zhou, S. S.; Han, J.; Srolovitz, D. J.; Haataja, M. P. Dynamic Phase Engineering of Bendable Transition Metal Dichalcogenide Monolayers. *Nano Lett.* **2017**, *17*, 2473−81.

(14) Zhang, C.; Kc, S.; Nie, Y.; Liang, C.; Vandenberghe, W. G.; Longo, R. C.; Zheng, Y.; Kong, F.; Hong, S.; Wallace, R. M.; Cho, K. Charge Mediated Reversible Metal−Insulator Transition in Monolayer $MoTe_2$ and $W_xMo_{1−x}Te_2$ Alloy. *ACS Nano* **2016**, *10*, 7370−5.

(15) Rhodes, D.; Chenet, D. A.; Janicek, B. E.; Nyby, C.; Lin, Y.; Jin, W.; Edelberg, D.; Mannebach, E.; Finney, N.; Antony, A.; Schiros, T.; Klarr, T.; Mazzoni, A.; Chin, M.; Chiu, Y. C.; Zheng, W.; Zhang, Q. R.; Ernst, F.; Dadayp, J. I.; Tong, X.; Ma, J.; Lou, R.; Wan, S.; Qian, T.; Ding, H.; Osgood, R. M.; Paley, D. W.; Lindenberg, A. M.; Huang, P. Y.; Pasupathy, A. N.; Dubey, M.; Hone, J.; Balicas, L. Engineering the Structural and Electronic Phases of $MoTe_2$ through W Substitution. *Nano Lett.* **2017**, *17*, 1616−22.

(16) Wang, Y.; Xiao, J.; Zhu, H.; Li, Y.; Alsaid, Y.; Fong, K. Y.; Zhou, Y.; Wang, S.; Shi, W.; Wang, Y.; Zettl, A.; Reed, E. J.; Zhang, X. Structural phase transition in monolayer $MoTe_2$ driven by electrostatic doping. *Nature* **2017**, *550*, 487−91.

(17) Song, S.; Keum, D. H.; Cho, S.; Perello, D.; Kim, Y.; Lee, Y. H. Room Temperature Semiconductor-Metal Transition of $MoTe_2$ Thin Films Engineered by Strain. *Nano Lett.* **2016**, *16*, 188−93.

(18) Lv, Y. Y.; Cao, L.; Li, X.; Zhang, B. B.; Wang, K.; Pang, B.; Ma, L. G.; Lin, D. J.; Yao, S. H.; Zhou, J.; Chen, Y. B.; Dong, S. T.; Liu, W. C.; Lu, M. H.; Chen, Y. L.; Chen, Y. F. Composition and temperature-dependent phase transition in miscible $Mo_{1−x}W_xTe_2$ single crystals. *Sci. Rep.* **2017**, *7*, 44587.

(19) Oliver, S. M.; Beams, R.; Krylyuk, S.; Kalish, I.; Singh, A. K.; Bruma, A.; Tavazza, F.; Joshi, J.; Stone, I. R.; Stranick, S. J.; Davydov, A. V.; Vora, P. M. The structural phases and vibrational properties of $Mo_{1-x}W_xTe_2$ alloys. *2D Mater.* **2017**, *4*, 045008.

(20) Li, Y.; Chernikov, A.; Zhang, X.; Rigosi, A.; Hill, H. M.; van der Zande, A. M.; Chenet, D. A.; Shih, E.-M.; Hone, J.; Heinz, T. F. Measurement of the optical dielectric function of monolayer transition-metal dichalcogenides: MoS_2, $MoSe_2$, WS_2, and WSe_2. *Phys. Rev. B: Condens. Matter Mater. Phys.* **2014**, *90*, 205422.

(21) Guo, H. H.; Yang, T.; Yamamoto, M.; Zhou, L.; Ishikawa, R.; Ueno, K.; Tsukagoshi, K.; Zhang, Z. D.; Dresselhaus, M. S.; Saito, R. Double resonance Raman modes in monolayer and few-layer $MoTe_2$. *Phys. Rev. B: Condens. Matter Mater. Phys.* **2015**, *91*, 205415.

(22) Luo, X.; Zhao, Y.; Zhang, J.; Toh, M.; Kloc, C.; Xiong, Q.; Quek, S. Y. Effects of lower symmetry and dimensionality on Raman spectra in two-dimensional WSe_2. *Phys. Rev. B: Condens. Matter Mater. Phys.* **2013**, *88*, 195313.

(23) Yamamoto, M.; Wang, S. T.; Ni, M. Y.; Lin, Y. F.; Li, S. L.; Aikawa, S.; Jian, W. B.; Ueno, K.; Wakabayashi, K.; Tsukagoshi, K. Strong Enhancement of Raman Scattering from a Bulk-Inactive Vibrational Mode in Few-Layer $MoTe_2$. *ACS Nano* **2014**, *8*, 3895−903.

(24) Scheuschner, N.; Gillen, R.; Staiger, M.; Maultzsch, J. Interlayer resonant Raman modes in few-layer MoS_2. *Phys. Rev. B: Condens. Matter Mater. Phys.* **2015**, *91*, 235409.

(25) Song, Q. J.; Tan, Q. H.; Zhang, X.; Wu, J. B.; Sheng, B. W.; Wan, Y.; Wang, X. Q.; Dai, L.; Tan, P. H. Physical origin of Davydov splitting and resonant Raman spectroscopy of Davydov components in multilayer $MoTe_2$. *Phys. Rev. B: Condens. Matter Mater. Phys.* **2016**, *93*, 115409.

(26) Grzeszczyk, M.; Golasa, K.; Zinkiewicz, M.; Nogajewski, K.; Molas, M. R.; Potemski, M.; Wysmolek, A.; Babinski, A. Raman scattering of few-layers $MoTe_2$. *2D Mater.* **2016**, *3*, 025010.

(27) Gołasa, K.; Grzeszczyk, M.; Molas, M. R.; Zinkiewicz, M.; Bala, Ł.; Nogajewski, K.; Potemski, M.; Wysmołek, A.; Babiński, A. Resonant quenching of Raman scattering due to out-of-plane A_{1g}/A'_1 modes in few-layer $MoTe_2$. *Nanophotonics* **2017**, *6*, 1281−8.

(28) Landau, L. D.; Lifshitz, E. M. *Mechanics*. 2nd ed.; Pergamon: Bristol, UK, 1969.

(29) Terrones, H.; Corro, E. D.; Feng, S.; Poumirol, J. M.; Rhodes, D.; Smirnov, D.; Pradhan, N. R.; Lin, Z.; Nguyen, M. A. T.; Elías, A. L.; Mallouk, T. E.; Balicas, L.; Pimenta, M. A.; Terrones, M. New First Order Raman-Active Modes in Few Layered Transition Metal Dichalcogenides. *Sci. Rep.* **2015**, *4*, 4215.

(30) Qiao, X.-F.; Li, X.-L.; Zhang, X.; Shi, W.; Wu, J.-B.; Chen, T.; Tan, P.-H. Substrate-free layer-number identification of two-dimensional materials: A case of $Mo_{0.5}W_{0.5}S_2$ alloy. *Appl. Phys. Lett.* **2014**, *106*, 223102.

(31) Su, W.-J.; Weng, W.-Q.; Wang, Y.-L.; Gan, W.-S.; Honda, S.-i.; Chen, R.-S.; Huang, Y.-S.; Lee, K.-Y. $Mo_{1−x}W_xS_2$-based photodetector fabrication and photoconductive characteristics. *Jpn. J. Appl. Phys.* **2017**, *56*, 032201.

(32) Zhang, M.; Wu, J.; Zhu, Y.; Dumcenco, D. O.; Hong, J.; Mao, N.; Deng, S.; Chen, Y.; Yang, Y.; Jin, C.; Chaki, S. H.; Huang, Y.-S.; Zhang, J.; Xie, L. Two-Dimensional Molybdenum Tungsten Diselenide Alloys: Photoluminescence, Raman Scattering, and Electrical Transport. *ACS Nano* **2014**, *8*, 7130−7.

(33) Chen, Y.; Dumcenco, D. O.; Zhu, Y.; Zhang, X.; Mao, N.; Feng, Q.; Zhang, M.; Zhang, J.; Tan, P.-H.; Huang, Y.-S.; Xie, L. Composition-dependent Raman modes of $Mo_{1−x}W_xS_2$ monolayer alloys. *Nanoscale* **2014**, *6*, 2833−9.

(34) Huang, L.-F.; Zeng, Z. Roles of Mass, Structure, and Bond Strength in the Phonon Properties and Lattice Anharmonicity of Single-Layer Mo and W Dichalcogenides. *J. Phys. Chem. C* **2015**, *119*, 18779−89.

(35) Froehlicher, G.; Lorchat, E.; Fernique, F.; Joshi, C.; Molina-Sanchez, A.; Wirtz, L.; Berciaud, S. Unified Description of the Optical Phonon Modes in N-Layer MoTe$_2$. *Nano Lett.* **2015**, *15*, 6481−9.

(36) Soubelet, P.; Bruchhausen, A. E.; Fainstein, A.; Nogajewski, K.; Faugeras, C. Resonance effects in the Raman scattering of monolayer and few-layer MoSe$_2$. *Phys. Rev. B: Condens. Matter Mater. Phys.* **2016**, *93*, 155407.

(37) Qiu, D. Y.; da Jornada, F. H.; Louie, S. G. Optical Spectrum of MoS$_2$: Many-Body Effects and Diversity of Exciton States. *Phys. Rev. Lett.* **2013**, *111*, 216805.

(38) Gillen, R.; Maultzsch, J. Light-Matter Interactions in Two-Dimensional Transition Metal Dichalcogenides: Dominant Excitonic Transitions in Mono- and Few-Layer MoX$_2$ and Band Nesting. *IEEE J. Sel. Top. Quantum Electron.* **2017**, *23*, 219.

(39) Wilson, J. A.; Yoffe, A. D. The transition metal dichalcogenides discussion and interpretation of the observed optical, electrical and structural properties. *Adv. Phys.* **1969**, *18*, 193−335.

(40) Beal, A. R.; Liang, W. Y.; Knights, J. C. Transmission spectra of some transition metal dichalcogenides: II. Group VIA: trigonal prismatic coordination. *J. Phys. C: Solid State Phys.* **1972**, *5*, 3540.

(41) Zhang, Y.; Chang, T. R.; Zhou, B.; Cui, Y. T.; Yan, H.; Liu, Z.; Schmitt, F.; Lee, J.; Moore, R.; Chen, Y.; Lin, H.; Jeng, H. T.; Mo, S. K.; Hussain, Z.; Bansil, A.; Shen, Z. X. Direct observation of the transition from indirect to direct bandgap in atomically thin epitaxial MoSe$_2$. *Nat. Nanotechnol.* **2014**, *9*, 111−5.

(42) Yun, W. S.; Han, S. W.; Hong, S. C.; Kim, I. G.; Lee, J. D. Thickness and strain effects on electronic structures of transition metal dichalcogenides: 2H-MX$_2$ semiconductors (M = Mo, W; X = S, Se, Te). *Phys. Rev. B: Condens. Matter Mater. Phys.* **2012**, *85*, 033305.

(43) Jin, W. C.; Yeh, P. C.; Zaki, N.; Zhang, D. T.; Sadowski, J. T.; Al-Mahboob, A.; van der Zande, A. M.; Chenet, D. A.; Dadap, J. I.; Herman, I. P.; Sutter, P.; Hone, J.; Osgood, R. M. Direct Measurement of the Thickness-Dependent Electronic Band Structure of MoS$_2$ Using Angle-Resolved Photoemission Spectroscopy. *Phys. Rev. Lett.* **2013**, *111*, 106801.

(44) Bromley, R. A.; M, R. B.; Yoffe, A. D. The band structures of some transition metal dichalcogenides. III. Group VIA: trigonal prism materials. *J. Phys. C: Solid State Phys.* **1972**, *5*, 759.

(45) Carvalho, A.; Ribeiro, R. M.; Neto, A. H. C. Band nesting and the optical response of two-dimensional semiconducting transition metal dichalcogenides. *Phys. Rev. B: Condens. Matter Mater. Phys.* **2013**, *88*, 115205.

(46) Mak, K. F.; Lee, C.; Hone, J.; Shan, J.; Heinz, T. F. Atomically Thin MoS$_2$: A New Direct-Gap Semiconductor. *Phys. Rev. Lett.* **2010**, *105*, 136805.

(47) Zhao, W.; Ghorannevis, Z.; Chu, L.; Toh, M.; Kloc, C.; Tan, P.-H.; Eda, G. Evolution of Electronic Structure in Atomically Thin Sheets of WS$_2$ and WSe$_2$. *ACS Nano* **2013**, *7*, 791−7.

(48) Liu, G. B.; Shan, W. Y.; Yao, Y. G.; Yao, W.; Xiao, D. Three-band tight-binding model for monolayers of group-VIB transition metal dichalcogenides. *Phys. Rev. B: Condens. Matter Mater. Phys.* **2013**, *88*, 085433.

(49) Rigosi, A. F.; Hill, H. M.; Rim, K. T.; Flynn, G. W.; Heinz, T. F. Electronic band gaps and exciton binding energies in monolayer Mo$_x$W$_{1-x}$S$_2$ transition metal dichalcogenide alloys probed by scanning tunneling and optical spectroscopy. *Phys. Rev. B: Condens. Matter Mater. Phys.* **2016**, *94*, 075440.

(50) Mak, K. F.; He, K.; Lee, C.; Lee, G. H.; Hone, J.; Heinz, T. F.; Shan, J. Tightly bound trions in monolayer MoS$_2$. *Nat. Mater.* **2013**, *12*, 207−11.

(51) Chernikov, A.; van der Zande, A. M.; Hill, H. M.; Rigosi, A. F.; Velauthapillai, A.; Hone, J.; Heinz, T. F. Electrical Tuning of Exciton Binding Energies in Monolayer WS$_2$. *Phys. Rev. Lett.* **2015**, *115*, 126802.

(52) Schmidt, R.; Niehues, I.; Schneider, R.; Druppel, M.; Deilmann, T.; Rohlfing, M.; de Vasconcellos, S. M.; Castellanos-Gomez, A.; Bratschitsch, R. Reversible uniaxial strain tuning in atomically thin WSe$_2$. *2D Mater.* **2016**, *3*, 021011.

(53) Robert, C.; Picard, R.; Lagarde, D.; Wang, G.; Echeverry, J. P.; Cadiz, F.; Renucci, P.; Hogele, A.; Amand, T.; Marie, X.; Gerber, I. C.; Urbaszek, B. Excitonic properties of semiconducting monolayer and bilayer MoTe$_2$. *Phys. Rev. B: Condens. Matter Mater. Phys.* **2016**, *94*, 155425.

(54) Jin, Z. H.; Li, X. D.; Mullen, J. T.; Kim, K. W. Intrinsic transport properties of electrons and holes in monolayer transition-metal dichalcogenides. *Phys. Rev. B: Condens. Matter Mater. Phys.* **2014**, *90*, 045422.

(55) Herring, C. Character tables for two space groups. *J. Franklin Inst.* **1942**, *233*, 525−43.

(56) Rhim, S. H.; Kim, Y. S.; Freeman, A. J. Strain-induced giant second-harmonic generation in monolayered 2H-MoX$_2$ (X = S, Se, Te). *Appl. Phys. Lett.* **2015**, *107*, 241908.

(57) Chang, C. H.; Fan, X. F.; Lin, S. H.; Kuo, J. L. Orbital analysis of electronic structure and phonon dispersion in MoS$_2$, MoSe$_2$, WS$_2$, and WSe$_2$ monolayers under strain. *Phys. Rev. B: Condens. Matter Mater. Phys.* **2013**, *88*, 195420.

(58) Shi, H. L.; Pan, H.; Zhang, Y. W.; Yakobson, B. I. Quasiparticle band structures and optical properties of strained monolayer MoS$_2$ and WS$_2$. *Phys. Rev. B: Condens. Matter Mater. Phys.* **2013**, *87*, 155304.

(59) Kormanyos, A.; Burkard, G.; Gmitra, M.; Fabian, J.; Zolyomi, V.; Drummond, N. D.; Fal'ko, V. k.p theory for two-dimensional transition metal dichalcogenide semiconductors. *2D Mater.* **2015**, *2*, 022001.

(60) Wang, Z. Y.; Zhou, Y. L.; Wang, X. Q.; Wang, F.; Sun, Q.; Guo, Z. X.; Jia, Y. Effects of in-plane stiffness and charge transfer on thermal expansion of monolayer transition metal dichalcogenide. *Chin. Phys. B* **2015**, *24*, 026501.

(61) Selig, M.; Berghauser, G.; Raja, A.; Nagler, P.; Schuller, C.; Heinz, T. F.; Korn, T.; Chernikov, A.; Malic, E.; Knorr, A. Excitonic linewidth and coherence lifetime in monolayer transition metal dichalcogenides. *Nat. Commun.* **2016**, *7*, 13279.

(62) Zhang, C. D.; Chen, Y. X.; Johnson, A.; Li, M. Y.; Li, L. J.; Mende, P. C.; Feenstra, R. M.; Shih, C. K. Probing Critical Point Energies of Transition Metal Dichalcogenides: Surprising Indirect Gap of Single Layer WSe$_2$. *Nano Lett.* **2015**, *15*, 6494−500.

(63) Ge, Y. F.; Wan, W. H.; Feng, W. X.; Xiao, D.; Yao, Y. G. Effect of doping and strain modulations on electron transport in monolayer MoS$_2$. *Phys. Rev. B: Condens. Matter Mater. Phys.* **2014**, *90*, 035414.

(64) Takagi, S. I.; Hoyt, J. L.; Welser, J. J.; Gibbons, J. F. Comparative study of phonon-limited mobility of two-dimensional electrons in strained and unstrained Si metal-oxide-semiconductor field-effect transistors. *J. Appl. Phys.* **1996**, *80*, 1567−77.

(65) Fischetti, M. V.; Laux, S. E. Band structure, deformation potentials, and carrier mobility in strained Si, Ge, and SiGe alloys. *J. Appl. Phys.* **1996**, *80*, 2234−52.

(66) del Corro, E.; Terrones, H.; Elias, A.; Fantini, C.; Feng, S. M.; Nguyen, M. A.; Mallouk, T. E.; Terrones, M.; Pimenta, M. A. Excited Excitonic States in 1L, 2L, 3L, and Bulk WSe$_2$ Observed by Resonant Raman Spectroscopy. *ACS Nano* **2014**, *8*, 9629−35.

■ NOTE ADDED AFTER ASAP PUBLICATION

This paper published ASAP on 3/29/2018. Figures 2 and 3 were enlarged, and the revised version was reposted on 4/2/2018.

Probing the Optical Properties and Strain-Tuning of Ultrathin $Mo_{1-x}W_xTe_2$

Ozgur Burak Aslan,*[a,e] Isha M. Datye,[b] Michal J. Mleczko,[b] Karen Sze Cheung,[a] Sergiy Krylyuk,[f,g] Alina Bruma,[f] Irina Kalish,[f] Albert V. Davydov,[f] Eric Pop,*[b,c,d] Tony F. Heinz,*[a,e]

[a]Department of Applied Physics, [b]Department of Electrical Engineering, [c]Department of Materials Science and Engineering, and [d]Precourt Institute for Energy, Stanford University, Stanford, California 94305, United States

[e]SLAC National Accelerator Laboratory, Menlo Park, California 94025, United States

[f]Material Measurement Laboratory, National Institute of Standards and Technology, Gaithersburg, Maryland 20899, United States

[g]Theiss Research, La Jolla, California 92037, United States

Corresponding Authors

*E-mails: oba2002@stanford.edu, tony.heinz@stanford.edu, epop@stanford.edu

1. Growth, Characterization, and Preparation of Samples

1.1 Growth of $Mo_{1-x}W_xTe_2$ crystals

$Mo_{1-x}W_xTe_2$ crystals are grown using the chemical vapor transport (CVT) method. $Mo_{1-x}W_xTe_2$ powders with a nominal composition of $x = 0.15$ are synthesized by reacting stoichiometric amounts of molybdenum (99.999%), tungsten (99.99%) and tellurium (99.9%) powders at 750 °C for 5 days in vacuum-sealed quartz ampoules. For single crystal growth, approximately 1.5 g of poly-crystalline $Mo_{1-x}W_xTe_2$ powder and 0.1 g of iodine as a transport agent (99.8%, 4.7 mg/cm^3) are placed in HF-etched and vacuum baked quartz ampoules. Following several argon flush-evacuation cycles, the ampoules are vacuum-sealed. The CVT growth is conducted at 1000 °C in a single-zone furnace for 7 days followed by ice-water quenching. The growth has produced monoclinic 1T'- $Mo_{1-x}W_xTe_2$ crystals that have been converted to the 2H phase by an additional vacuum annealing at 750 °C for 72 hours, followed by cooling to room temperature at a 10 °C/hour rate.

1.2 Growth of $MoTe_2$ crystals

$MoTe_2$ crystals are also grown using the CVT method. $MoTe_2$ molecular powder (ESPI Metals $MoTe_2$, 99.9%) is sealed in quartz ampoules with elemental iodine added as a transport agent (Alfa Aesar, 99.99+%) at 5 mg/cm^3. Ampoules are repeatedly purged and evacuated under argon before sealing. The crystals are grown for 14 days along a ~11 cm transport length, representing a 100 °C thermal gradient from a source hot zone kept at 800 °C.

1.3 Characterization of Crystals

Crystal phases of obtained $Mo_{1-x}W_xTe_2$ alloys are determined by powder X-ray diffraction (XRD) and aberration-corrected high angle annular dark field scanning transmission electron microscopy (Cs-corrected HAADF-STEM). HAADF-STEM images are recorded on an aberration-corrected FEI Titan 80-300 operating at 300 kV. The $Mo_{1-x}W_xTe_2$ crystals are crushed in ethanol and a drop of solution is deposited onto an amorphous Carbon (a-C) coated TEM grid (Agar Inc.). HAADF-STEM images are collected at a camera length of 100 mm corresponding to inner and outer collection angles of 70.6 and 399.5 mrad respectively.

The XRD patterns of the powdered $Mo_{1-x}W_xTe_2$ crystals have been obtained in the range of 10° to 105° 2θ using a Philips X-ray diffractometer in the Bragg-Brentano geometry with CuKα radiation. Figure S1 is an extended version of the XRD spectra shown in Figure 1a in the main text. Experimental lattice parameters are refined using the Materials Data, Inc., JADE 6.1 XRD Patterns Processing software (MDI JADE 6.1).

The chemical composition of $Mo_{1-x}W_xTe_2$ alloys is determined using energy-dispersive X-ray spectroscopy (EDS) in JEOL JSM-7100F field emission scanning electron microscope (FESEM) equipped with an Oxford Instruments X-Max 80 EDS detector. For quantitative analysis, EDS spectra are acquired from several 1x1 μm^2 areas on the sample at the following conditions: accelerating voltage 10 kV, working distance 10 mm, processing time 60 seconds with 15% deadtime. Spectra, as exemplified in Figure S2, have been fit and quantified using the AZtec software package in standardless mode.
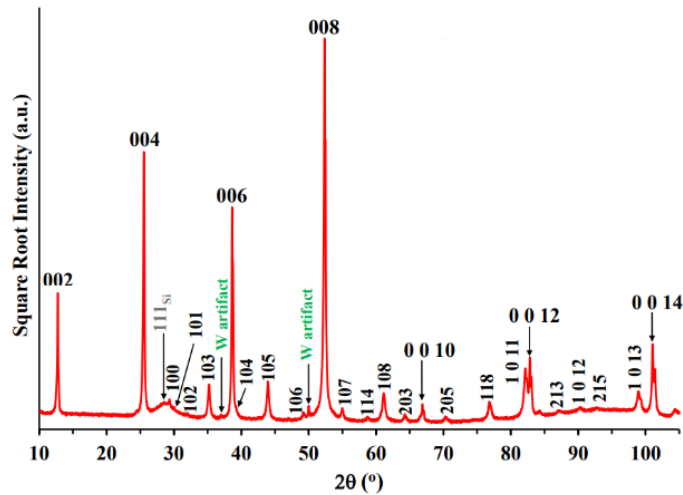
Figure S1: Extended version of the XRD scan for the $Mo_{0.91}W_{0.09}Te_2$ sample, shown in Figure 1a in the main text. Experimental lattice parameters for the 2H crystal structure (space group $P6_3/mmc$) are: a=3.5192(6) Å, c=13.9728(14) Å. These values agree with the literature data for $MoTe_2$ compound: a=3.5182(14) Å and c=13.9736(40) Å.[1]

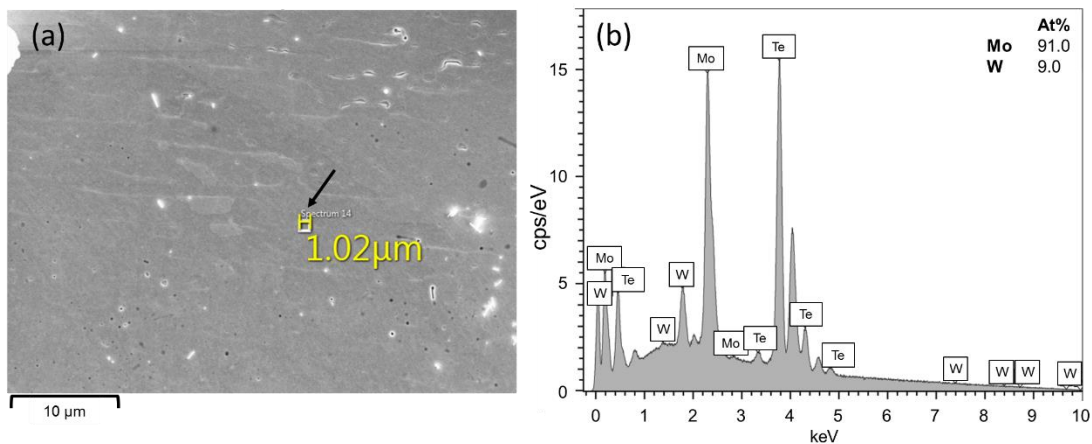Figure S2: (a) SEM plan-view image of 2H-$Mo_{0.91}W_{0.09}Te_2$ sample surface. The black arrow points to the EDS spectrum sampled over ~1 μm^2 area. (b) Corresponding EDS spectrum measuring the 9±1 atomic % W. Comment: the Te/(Mo+W) ratio in this sample has been measured to be 1.98±0.02, which corresponds to the $Mo_{0.91}W_{0.09}Te_{1.98}$ composition. Note that for simplicity, the Te content in the formula is rounded to 2.0 and thus the alloy is represented by the $Mo_{0.91}W_{0.09}Te_2$ composition throughout this study.

1.4 Preparation of Samples

For the optical measurements without strain, we exfoliate $MoTe_2$ and $Mo_{0.91}W_{0.09}Te_2$ from bulk crystals onto ~1 mm thick polydimethylsiloxane (PDMS) substrates (base: curing agent ratios of 10.5:1 by volume) to obtain ultrathin flakes. The thicknesses of the atomically thin crystals are determined by Raman spectroscopy,[2] and optical contrast.

For the optical measurements with strain, we transfer monolayer (1L) crystals from PDMS to ~0.25 mm thick polyethylene naphthalate (PEN) flexible plastic substrates using a stage heated to 40 °C with a micromanipulator to precisely position the crystals in the middle of the PEN substrate. We press the PDMS onto the PEN using the micromanipulator and keep it in contact for 1 to 2 minutes. We slowly release the PDMS from the PEN, ensuring that the crystals do not break during the transfer.

The mechanical exfoliation is performed in ambient atmosphere and the transfer process to PEN is carried out in a N_2 glove box with generally <3 ppm O_2 and H_2O. Metal strips (10 nm Cr/30 nm Ag) are then patterned by electron beam (e-beam) lithography and deposited by e-beam evaporation onto the crystals to clamp them to the substrate, as shown in Figure S3a and Figure S3b. We also spin-coat ~100 nm polymethyl methacrylate (PMMA) onto the $Mo_{0.91}W_{0.09}Te_2$ samples to act as an additional clamping layer, as well as an oxygen and moisture barrier. We have not observed degradation of the $MoTe_2$ and $Mo_{0.91}W_{0.09}Te_2$ samples during Raman or PL measurements on the time scale of days to weeks.

We apply in-plane uniaxial tensile strain using a two-point bending apparatus. The strain, ϵ, is calculated as $\epsilon = \tau/(2R)$, where τ = 250 μm is the thickness of the PEN and R is the radius of curvature of the bent substrate, determined from photos taken at each strain level (Figure S3c).

We use PEN or polyethylene terephthalate glycol-modified (PETG) substrates for the optical measurements on the bending platform with strain (Figure S3) due to their high Young's moduli of ~5 GPa.[3-4]
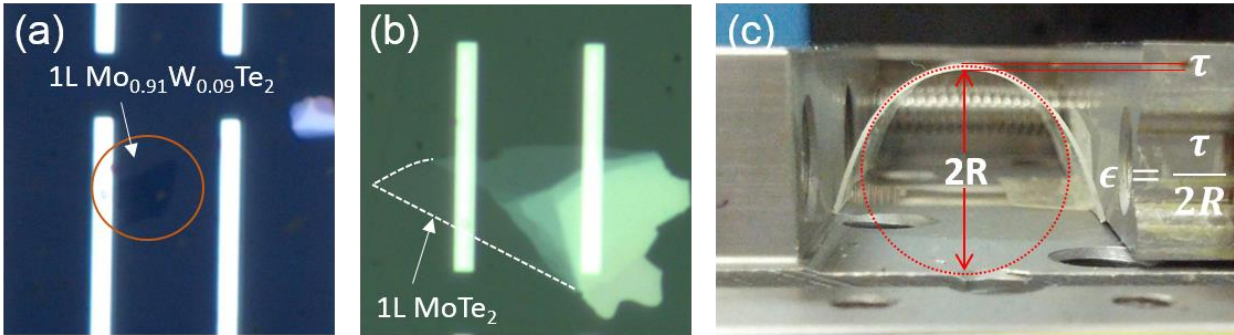

Figure S3: Optical image of (a) $Mo_{0.91}W_{0.09}Te_2$ and (b) $MoTe_2$ clamped to PEN with metal strips. (c) Two-point bending apparatus used for applying tensile strain. The strain is calculated from the formula shown, with the radius of curvature determined from the photo taken at each strain level.

2. Details on the Optical Measurements

The Raman spectroscopy measurements are performed with a commercial micro-Raman setup (Horiba Labram) in a backscattering geometry. A 100× objective (NA = 0.9) is used to collect the scattered photons, which are analyzed in a spectrometer equipped with a grating of 1800 lines/mm. The laser power on the samples is about 70 µW (for 532 nm excitation), 130 µW (for 633 nm excitation), and 200 µW (for 785 nm excitation), which is sufficient for obtaining a good signal-to-noise ratio. To ensure we do not damage the samples with these laser powers, we check the crystals optically for any visible damage between measurements and we also confirm that the intensities of the Raman peaks do not reduce over time. These measurements do not induce heating in the samples; we compare lower laser power measurements to higher laser power measurements to check for peak shifting which would imply heating.

The reflection contrast presented in the main text is calculated as $\Delta R/R = (R_{MoWTe2+substrate} - R_{substrate})/R_{substrate}$ where $R_{MoWTe2+substrate}$ and $R_{substrate}$ represent the reflectance of the thin $Mo_{0.91}W_{0.09}Te_2$ sample on the substrate and of the bare substrate, respectively. For a sample with sufficiently small absorbance on a thick transparent substrate, as in our case, we can determine the absorbance $\mathcal{A}$ of the unsupported thin $Mo_{0.91}W_{0.09}Te_2$ from $\Delta R/R$ as $\mathcal{A} = \frac{1}{4}(n_{substrate}^2 - 1)(\frac{\Delta R}{R})$,[5-7] where $n_{substrate}$ denotes the refractive index of the substrate.[8] We can thus probe the absorption spectra of sufficiently thin samples through measurements of their reflection contrast.

The reflection contrast setup consists of a quartz tungsten halogen source combined with a microscope using 100× objectives (NA = 0.95 and 0.9). The reflected light from the sample is dispersed by a monochromator onto a Peltier cooled Si or liquid-nitrogen cooled InGaAs CCD array. The peak positions and spectral widths (full width at half maximum) of the reflectance contrast measurements are extracted by fitting multiple Lorentzian line-shapes to the experimental data.

Photoluminescence (PL) measurements are performed in the same setup as reflection contrast with a 100× objective (NA = 0.95) to collect the backscattered emission. For excitation, we use a 633 nm (HeNe) or a 671 nm (solid-state) laser. The excitation power level is around 10 µW. Backscattered laser radiation is suppressed by a long-pass filter in front of the monochromator.

The Raman measurements are performed on PDMS substrates, while the absorption and PL measurements are performed on PDMS and PETG substrates. All optical measurements are performed in ambient conditions.

3. Raman Spectroscopy of MoTe$_2$

The Raman spectra of 1L to 4L and bulk MoTe$_2$ with excitation wavelengths of 532 nm, 633 nm, and 785 nm are shown in Figure S4. The peak positions for 1L and 2L MoTe$_2$ and Mo$_{0.91}$W$_{0.09}$Te$_2$ using all three lasers are shown in Table S1.
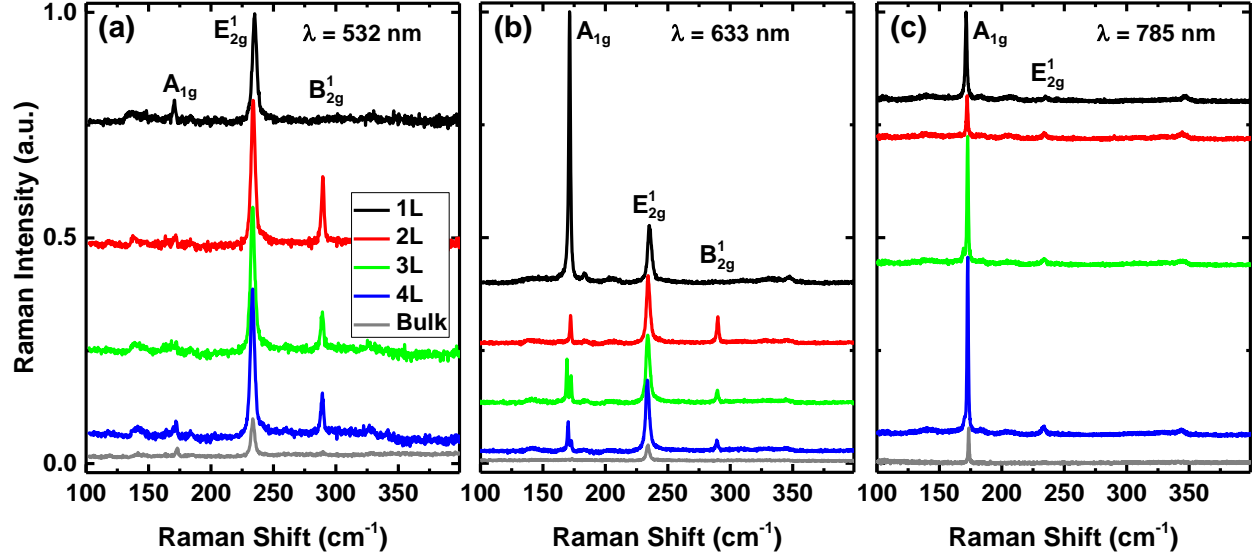

Figure S4: Raman spectra of 1L to 4L and bulk MoTe$_2$ (modes labeled according to bulk notation) using laser excitation wavelengths of (a) 532 nm, (b) 633 nm, and (c) 785 nm. The spectra are offset for clarity.

Table S1. Raman peak positions of 1L and 2L MoTe$_2$ vs. Mo$_{0.91}$W$_{0.09}$Te$_2$ using laser excitation wavelengths of 532 nm, 633 nm, and 785 nm. All peak positions are in cm^{-1}. The modes are labeled according to the bulk notation (see main text for correct 1L and few-layer notations).

Wavelength of Laser	Mode	1L		2L	
		MoTe$_2$	Mo$_{0.91}$W$_{0.09}$Te$_2$	MoTe$_2$	Mo$_{0.91}$W$_{0.09}$Te$_2$
532 nm	A$_{1g}$	171.5	171.8		
	E$^1_{2g}$	235.5	236.6	234.6	234.5
	B$^1_{2g}$			290.3	289.3
633 nm	A$_{1g}$	171.0	171.8	171.7	172.5
	E$^1_{2g}$	235.0	236.1	233.9	234.4
	B$^1_{2g}$			289.5	289.1
785 nm	A$_{1g}$	171.3	172.2	172.2	172.8
	E$^1_{2g}$	234.9		234.3	234.6

4. Rate of Band Gap Shift with Strain

We have measured PL from a few different regions on 1L $Mo_{0.91}W_{0.09}Te_2$ and $MoTe_2$ at each level of strain. In the case of $MoTe_2$, we have found that regions with one metal clamp (left of the leftmost clamp) and regions between the two metal clamps (see Figure S3b) yielded similar values of band gap shift per % strain. From these measurements, we have concluded that one metal clamp was sufficient to ensure that the sample was clamped to the substrate, as in the case of $Mo_{0.91}W_{0.09}Te_2$ (see Figure S3a). We also note that our measurements of PL peak energy with strain (Figure S6) are nearly linear, suggesting that our samples did not slip along the substrate with increasing strain.

We note that a trend similar to the band gaps (energy difference between the K point of the valence band and K point of the conduction band, K-K gap) of MoS_2, $MoSe_2$, $MoTe_2$ (MoS_2>$MoSe_2$>$MoTe_2$) is expected in the rates of the band gap shifts with tensile strain.[9-10] We plot the calculations by Rhim *et al*.[10] by assuming that uniaxial strain redshifts the band gap at half the rate of biaxial strain (see Figure S5a).[11] We obtain from their calculations that the band gaps of MoS_2, $MoSe_2$, $MoTe_2$ redshift at a rate of about 55, 50, 37 meV/% strain, respectively. Recent studies on 1L $MoSe_2$ and MoS_2 yielded similar results of about 40 to 50 meV/% strain.[12-13]

Based on the discussion above, we believe that the high strain of ~2.3% we have achieved via metal clamps is an indication that the samples have been sufficiently clamped to the substrates. A similar value of ~2.1% strain achieved via polymer clamping was reported by Desai *et al*.[14]
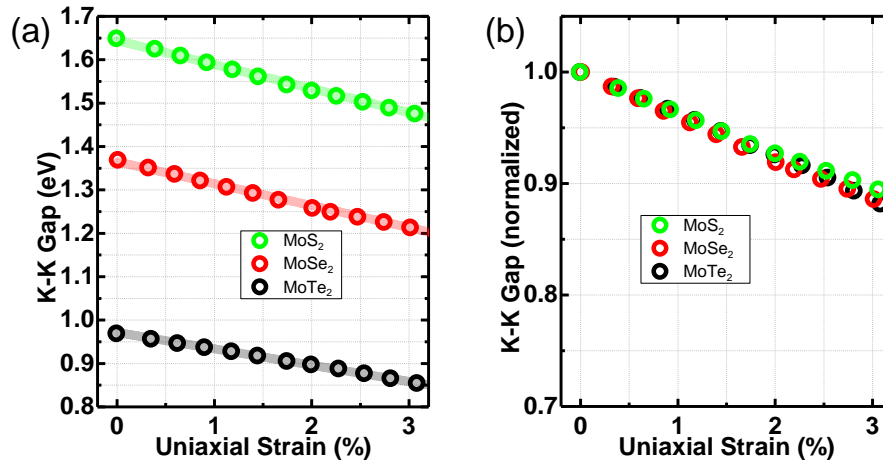

Figure S5: (a) Absolute and (b) normalized K-K gaps of MoS_2, $MoSe_2$, $MoTe_2$ with increasing uniaxial tensile strain (adapted from the calculations by Rhim *et al*.[10]). The calculations suggest that band gaps of MoS_2, $MoSe_2$, and $MoTe_2$ redshift at a rate of about 55, 50, 37 meV/% strain, respectively.

5. Peak Positions and Spectral Widths of Strain-Dependent PL Measurements on 1L MoTe$_2$ and Mo$_{0.91}$W$_{0.09}$Te$_2$
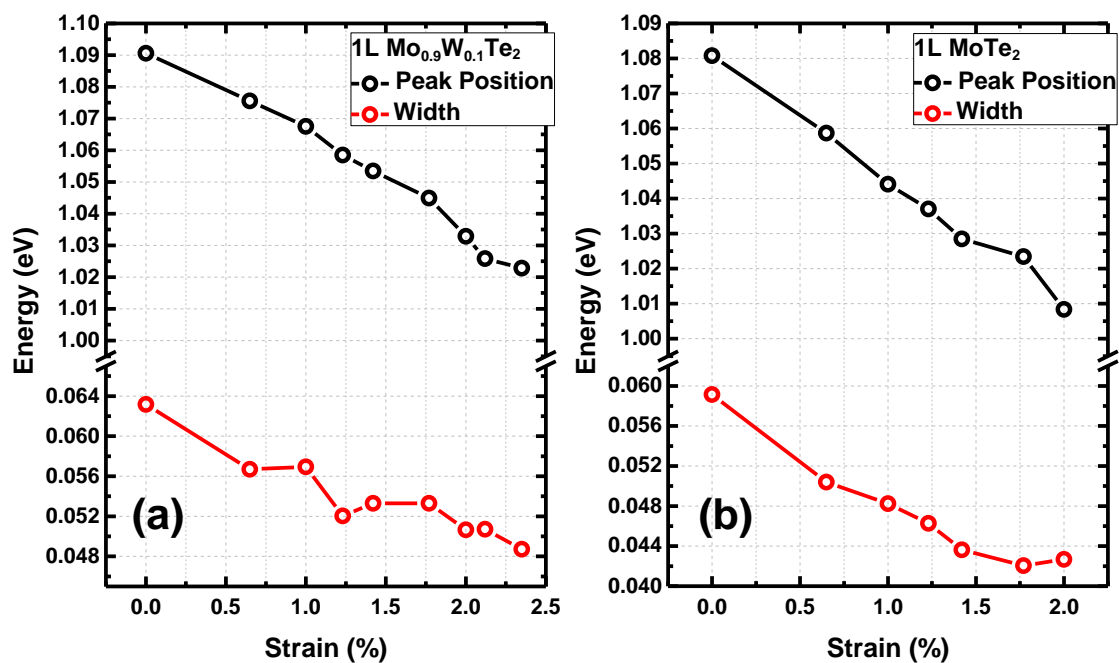

Figure S6: Peak positions and line widths of the strain-dependent PL spectra shown in Figure 4 in the main text for (a) 1L Mo$_{0.91}$W$_{0.09}$Te$_2$ and (b) 1L MoTe$_2$.

Figure S6 shows the peak positions and widths of the strain-dependent PL spectra shown in Figure 4 in the main text for 1L Mo$_{0.91}$W$_{0.09}$Te$_2$ and 1L MoTe$_2$.

6. Strain-Dependent Absorption and PL Measurements on 1L $Mo_{0.91}W_{0.09}Te_2$

We perform strain-dependent absorption and PL measurements on 1L $Mo_{0.91}W_{0.09}Te_2$ to verify that the decrease in the spectral linewidth with strain is visible in the absorption as well as the PL spectra (reported in the main text).

We exfoliate the 1L on a ~1 mm thick polydimethylsiloxane (PDMS) substrate and transfer the 1L onto a ~1 mm (PETG) substrate at ~40 °C. Next, we perform the strain measurements. We have also performed measurements immediately before and after the transfer to ensure that the line widths of the optical transitions of interest have not been significantly altered during sample preparation. Our sample preparation is performed in ambient conditions and includes no chemicals in order to keep the sample intact. All the fabrication and measurements listed above have been completed within 24 hours.
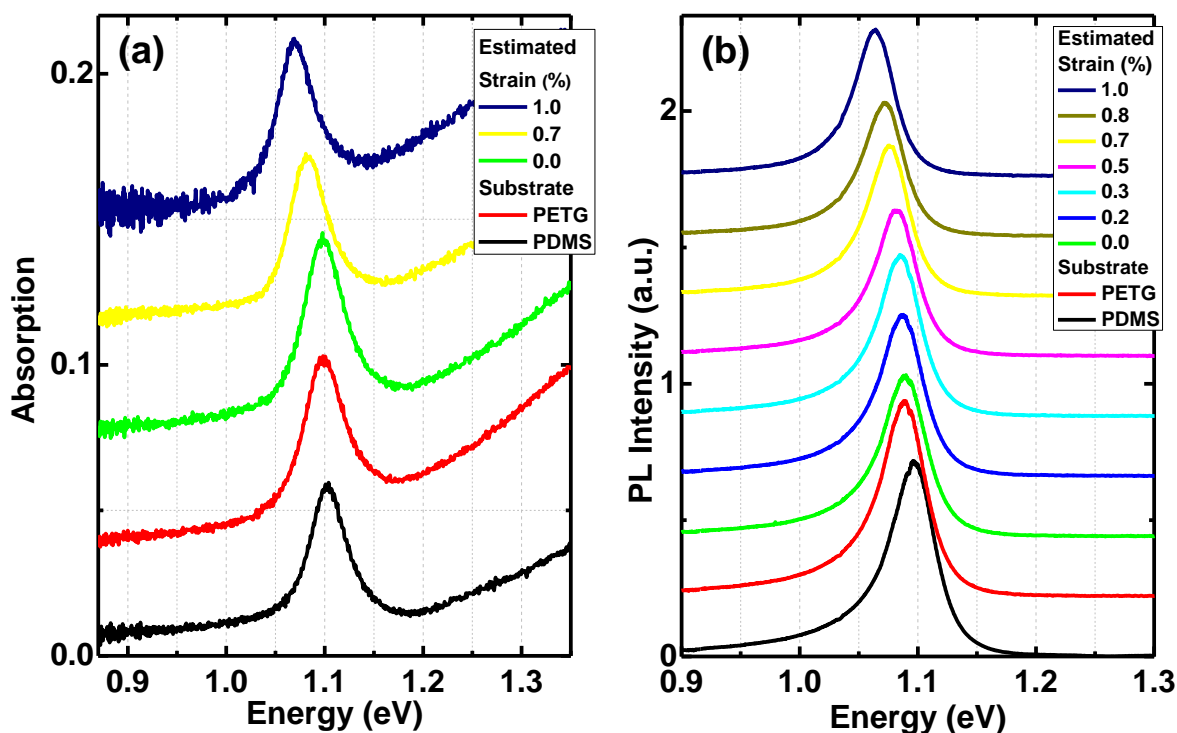

Figure S7: Strain-dependent (a) absorption and (b) PL measurements of 1L $Mo_{0.91}W_{0.09}Te_2$ on PDMS (as-exfoliated, before transferring onto PETG), on PETG (after transfer) and with increasing strain. The spectra are vertically offset. Intensities of the measurements on PDMS were adjusted to match the PETG due to their different refractive indices which result in different electric field enhancement on their surfaces.

Figure S7 contains the absorption and PL spectra we obtained. We analyze the spectra and extract the peak positions and the spectral widths in the following way: We fit the absorption spectra in the vicinity of the A exciton to two Lorentzians, one for the A exciton and one accounting for the higher energy transitions. For the PL spectra, we look for the energy at which the spectrum is maximized and then obtain the width accordingly.
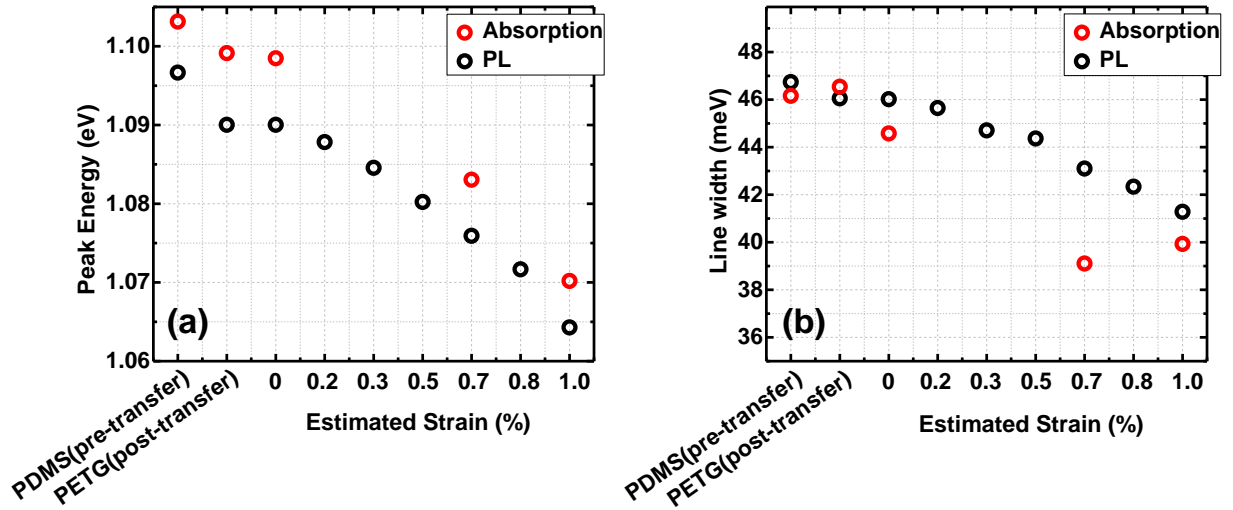
Figure S8: (a) Peak energy and (b) Line widths of absorption and PL spectra corresponding to Figure S7.

We present the extracted results in Figure S8. We note that the absorption and PL peak energy on PDMS and PETG (before and after the transfer, respectively) are slightly offset from each other. This is likely due to a small initial strain in the 1L $Mo_{0.91}W_{0.09}Te_2$, which may have been induced during the transfer, before external strain is applied.

The strain levels in the measurements shown in Figure S7 and Figure S8 are estimated after obtaining the shift in peak positions and comparing them to typical shifts with strain of several other measurements. The accuracy of the estimates does not alter the claims made in this text or in the main text.

We observe that the peak positions in both types of spectra decrease with strain. More importantly, the widths decrease in both spectra from ~47 meV down to about 39 meV to 40 meV (absorption) and ~41 meV (PL) at the highest strain achieved.

Now, we consider the effect of trions on absorption: The density of states is much higher for excitons than trions, and the formation of a trion requires the additional step of binding one quasi-free electron or hole. Thus, the absorption process is mainly governed by excitons (unlike PL as stated in the main text). Therefore, we infer that the narrowing of the spectral widths is not expected to stem from the suppression of the PL.

Similar to the case of trions, emission by shallow trap states may contribute to PL and give rise to lineshapes that are asymmetric at the lower energy side (which is the case as seen in Figure S7b), but they are not expected to contribute to the absorption. Absorption spectra are indeed found to be symmetric, (after subtracting the absorption due to higher lying transitions) reflecting the lack of contribution from shallow trap states. Therefore, shallow trap states cannot explain the observed strain-induced linewidth narrowing in the absorption spectra.

Figure S8 shows that the spectral linewidths at 0.0% and 1.0% strain are about $\Gamma(\epsilon = 0.0\%)$ = 47 meV and $\Gamma(\epsilon = 1.0\%)$ = 41 meV, respectively. The change in linewidth is then $\Delta\Gamma$ = 6 meV. If we express the total linewidth, Γ, as follows:

$$\Gamma = \Gamma_{rad} + \Gamma_{K-Q} + \Gamma_{K-K} \tag{1}$$

Where Γ_{rad}, Γ_{K-Q} and Γ_{K-K} are contributions to the linewidth broadening due to the radiative decay, exciton-phonon intervalley scattering from K to Q valley, and intravalley scattering within the K valley, respectively.[8,15] Assuming Γ_{rad} and Γ_{K-K} change only insignificantly with 1.0% strain, we conclude that Γ_{K-Q} is larger than about 6 meV.[16] Therefore, an upper limit on the lifetime of the exciton-phonon scattering from K to Q of 1L MoTe$_2$ and Mo$_{0.91}$W$_{0.09}$Te$_2$, τ_{K-Q}, can be estimated as follows:

$$\tau_{K-Q} = \frac{\hbar}{\Gamma_{K-Q}} \lesssim 110 \, fs \tag{2}$$

7. Comparison of Electrical Transport Properties of Few-Layer $Mo_{0.91}W_{0.09}Te_2$ and $MoTe_2$
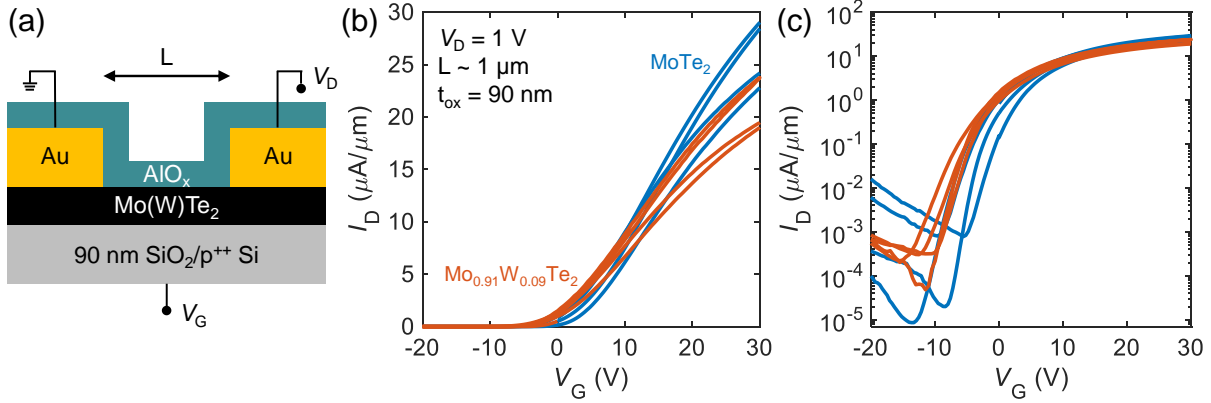

Figure S9: (a) Device cross-section diagram. (b) Linear and (c) log scale plots showing measured drain current (I_D) vs. gate voltage (V_G) transfer curves of two few-layer $Mo_{0.91}W_{0.09}Te_2$ (red) and two few-layer $MoTe_2$ (blue) transistors with channel lengths of ~1 μm. The double curves show the forward and backward I_D-V_G sweeps.

We have performed preliminary electron transport measurements of few-layer (3-12 nm) $MoTe_2$ and $Mo_{0.91}W_{0.09}Te_2$ transistors. All devices have channel lengths of ~1 μm, Au source/drain contacts, 90 nm SiO_2/Si (p^{++}) back gates, and 20 nm aluminum oxide (AlO_x) capping layers (see Figure S9a for a schematic of the devices). Figure S9b,c show comparisons of their drain current (I_D) vs. gate voltage (V_G) transfer curves. Without accounting for contact resistance, the estimated field-effect mobilities of the $MoTe_2$ transistors are μ_{FE} ~32 cm^2/(Vs) and ~26 cm^2/(Vs), and for $Mo_{0.91}W_{0.09}Te_2$ transistors μ_{FE} ~24 cm^2/(Vs) and ~20 cm^2/(Vs). The $MoTe_2$ transistors tend to have higher maximum drive currents at V_G = 30 V, despite a slightly higher threshold voltage (see Figure S9). However, given differences in thickness and variability in contact resistance (well-known with TMDC transistors),[17] it is difficult to determine whether $Mo_{0.91}W_{0.09}Te_2$ has poorer transport properties compared to $MoTe_2$; such sample-to-sample variation can be seen even among nominally "identical" TMDC transistors. Further measurements must be performed on $Mo_{1-x}W_xTe_2$ devices with multiple channel lengths, contact metals, and compositions to draw more definitive conclusions and to exclude any differences stemming from device-to-device variation.

8. References

(1) Knop, O.; Macdonald, R. D. Chalkogenides of Transition Elements .3. Molybdenum Ditelluride. *Can. J. Chem.* **1961,** *39*, 897-904.

(2) Ruppert, C.; Aslan, O. B.; Heinz, T. F. Optical Properties and Band Gap of Single- and Few-layer MoTe$_2$ Crystals. *Nano Lett.* **2014,** *14*, 6231-6.

(3) Liu, Z.; Amani, M.; Najmaei, S.; Xu, Q.; Zou, X. L.; Zhou, W.; Yu, T.; Qiu, C. Y.; Birdwell, A. G.; Crowne, F. J.; Vajtai, R.; Yakobson, B. I.; Xia, Z. H.; Dubey, M.; Ajayan, P. M.; Lou, J. Strain and structure heterogeneity in MoS$_2$ atomic layers grown by chemical vapour deposition. *Nat. Commun.* **2014,** *5*, 5246.

(4) Jiang, T.; Huang, R.; Zhu, Y. Interfacial Sliding and Buckling of Monolayer Graphene on a Stretchable Substrate. *Adv. Funct. Mater.* **2014,** *24*, 396-402.

(5) Mak, K. F.; Sfeir, M. Y.; Wu, Y.; Lui, C. H.; Misewich, J. A.; Heinz, T. F. Measurement of the Optical Conductivity of Graphene. *Phys. Rev. Lett.* **2008,** *101*, 196405.

(6) Mcintyre, J. D.; Aspnes, D. E. Differential Reflection Spectroscopy of Very Thin Surface Films. *Surf. Sci.* **1971,** *24*, 417-34.

(7) Buckley, R. G.; Beaglehole, D. Absorptance of Thin-Films. *Appl. Opt.* **1977,** *16*, 2495-9.

(8) Cai, Z.; Qiu, W.; Shao, G.; Wang, W. A new fabrication method for all-PDMS waveguides. *Sens. Actuators. A Phys.* **2013,** *204*, 44-7.

(9) Zeng, F.; Zhang, W. B.; Tang, B. Y. Electronic structures and elastic properties of monolayer and bilayer transition metal dichalcogenides MX$_2$ (M = Mo, W; X = O, S, Se, Te): A comparative first-principles study. *Chin. Phys. B* **2015,** *24*, 097103.

(10) Rhim, S. H.; Kim, Y. S.; Freeman, A. J. Strain-induced giant second-harmonic generation in monolayered 2H-MoX$_2$ (X = S, Se, Te). *Appl. Phys. Lett.* **2015,** *107*, 241908.

(11) Plechinger, G.; Castellanos-Gomez, A.; Buscema, M.; van der Zant, H. S. J.; Steele, G. A.; Kuc, A.; Heine, T.; Schuller, C.; Korn, T. Control of biaxial strain in single-layer molybdenite using local thermal expansion of the substrate. *2D Mater.* **2015,** *2*, 015006.

(12) Conley, H. J.; Wang, B.; Ziegler, J. I.; Haglund, R. F.; Pantelides, S. T.; Bolotin, K. I. Bandgap Engineering of Strained Monolayer and Bilayer MoS$_2$. *Nano Lett.* **2013,** *13*, 3626-30.

(13) Ji, J. T.; Zhang, A. M.; Xia, T. L.; Gao, P.; Jie, Y. H.; Zhang, Q.; Zhang, Q. M. Strain-modulated excitonic gaps in mono- and bi-layer MoSe$_2$. *Chin. Phys. B* **2016,** *25*, 077802.

(14) Desai, S. B.; Seol, G.; Kang, J. S.; Fang, H.; Battaglia, C.; Kapadia, R.; Ager, J. W.; Guo, J.; Javey, A. Strain-Induced Indirect to Direct Bandgap Transition in Multilayer WSe$_2$. *Nano Lett.* **2014,** *14*, 4592-7.

(15) Selig, M.; Berghauser, G.; Raja, A.; Nagler, P.; Schuller, C.; Heinz, T. F.; Korn, T.; Chernikov, A.; Malic, E.; Knorr, A. Excitonic linewidth and coherence lifetime in monolayer transition metal dichalcogenides. *Nat. Commun.* **2016,** *7*, 13279.

(16) Feierabend, M.; Morlet, A.; Berghauser, G.; Malic, E. Impact of strain on the optical fingerprint of monolayer transition-metal dichalcogenides. *Phys. Rev. B* **2017,** *96*, 045425.

(17) English, C. D.; Shine, G.; Dorgan, V. E.; Saraswat, K. C.; Pop, E. Improved contacts to MoS$_2$ transistors by ultra-high vacuum metal deposition. *Nano Lett.* **2016,** *16*, 3824-30.